J. Fluid Mech. (2010), *vol.* 644, *pp.* 321–336.
doi:10.1017/S0022112009992503

High-mode stationary waves in stratified flow over large obstacles

JODY M. KLYMAK[1]†, SONYA M. LEGG[2] AND ROBERT PINKEL[3]

[1]Department of Physics and Astronomy, University of Victoria, Victoria, Canada V8W 3P6

[2]Program in Atmosphere and Ocean Sciences, Princeton University, Princeton, NJ 08544, USA

[3]Scripps Institution of Oceanography, University of California, San Diego, La Jolla, CA 98105, USA

(Received 20 October 2008; revised 28 September 2009; accepted 28 September 2009)

Simulations of steady two-dimensional stratified flow over an isolated obstacle are presented where the obstacle is tall enough so that the topographic Froude number, $Nh_m/U_o \gg 1$. N is the buoyancy frequency, h_m the height of the topography from the channel floor and U_o the flow speed infinitely far from the obstacle. As for moderate Nh_m/U_o ($\sim$1), a columnar response propagates far up- and downstream, and an arrested lee wave forms at the topography. Upstream, most of the water beneath the crest is blocked, while the moving layer above the crest has a mean velocity $U_m = U_o H/(H - h_m)$. The vertical wavelength implied by this velocity scale, $\lambda_o = 2\pi U_m/N$, predicts dominant vertical scales in the flow. Upstream of the crest there is an accelerated region of fluid approximately λ_o thick, above which there is a weakly oscillatory flow. Downstream the accelerated region is thicker and has less intense velocities. Similarly, the upstream lift of isopycnals is greatest in the first wavelength near the crest, and weaker above and below. Form drag on the obstacle is dominated by the blocked response, and not on the details of the lee wave, unlike flows with moderate Nh_m/U_o.

Directly downstream, the lee wave that forms has a vertical wavelength given by λ_o, except for the deepest lobe which tends to be thicker. This wavelength is small relative to the fluid depth and topographic height, and has a horizontal phase speed $c_{px} = -U_m$, corresponding to an arrested lee wave. When considering the spin-up to steady state, the speed of vertical propagation scales with the vertical component of group velocity $c_{gz} = \alpha U_m$, where α is the aspect ratio of the topography. This implies a time scale $\hat{t} = tN\alpha/2\pi$ for the growth of the lee waves, and that steady state is attained more rapidly with steep topography than shallow, in contrast with linear theory, which does not depend on the aspect ratio.

1. Introduction

Nonlinear lee waves are observed in the atmosphere as downslope flows over mountain ranges (i.e. Lilly 1978) and in the ocean as flow over sills (i.e. Farmer & Smith 1980). These flows have been studied in the field, laboratories, and numerically (see Baines 1995 for a comprehensive review). These studies, however, have usually been for flows where the lee wave is of similar scale to the obstacle (or even much

† Email address for correspondence: jklymak@uvic.ca

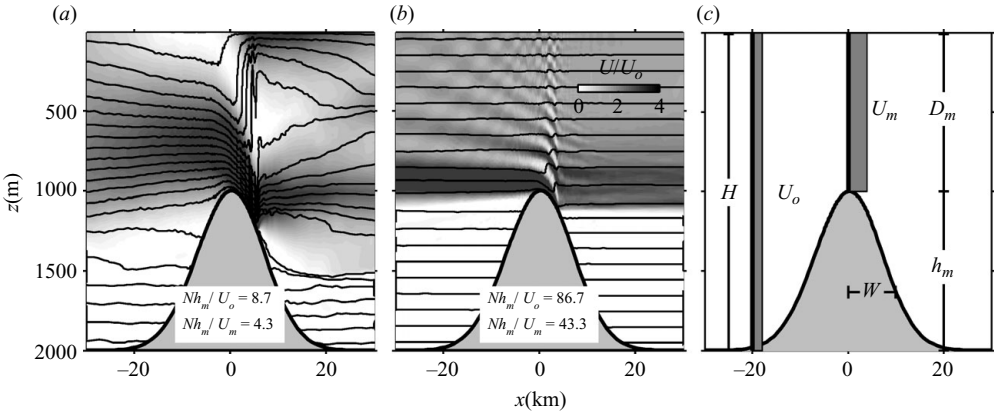

FIGURE 1. (*a*) Steady state of moderate Nh_m/U_o flow (i.e. low mode, but still blocked upstream). (*b*) High Nh_m/U_o flow (i.e. high mode) characteristic of tidal flow over deep ocean ridges. (*c*) Sketch of flow parameters. The mean flow in all cases is in the positive-x direction.

larger), meaning that in a finite-depth fluid they are dominated by low vertical modes in the flow (i.e. figure 1*a*).

Recently, lee waves made up of high vertical modes have been observed at underwater ridges and continental shelves. Large-amplitude nonlinear waves were observed breaking near the crest of the underwater ridge between Oahu and Kauii (Levine & Boyd 2006; Klymak, Pinkel & Rainville 2008). These breaking waves led to vertical displacements of over 100 m, and drove large viscous dissipation and mixing. Since the vertical wavelength was only a fraction of the local water depth and obstacle height, we loosely term them 'high mode'. Recent numerical work demonstrates that these high-mode waves are formed at the topographic break during off-ridge tidal flow (Legg & Klymak 2008). When the tide reverses the waves propagate on-ridge, much like lee waves released from tidal flows over sills in fjords (Farmer & Smith 1980; Klymak & Gregg 2003). Similar phenomena have been implicated in mixing on the Oregon continental slope (Nash *et al.* 2007).

In this paper, we step back from oscillating forcing and consider the response of a large obstacle to steady forcing. The goal is to predict the lee response, in particular the amplitude of the lee wave. We are also interested in understanding how long it takes for the lee wave to establish itself, since, if the flow is oscillating and the establishment time is large compared to the forcing period, the arrested lee wave may not be observed.

We consider channel flow with a depth H, stratification N and an initial barotropic velocity of U_o (figure 1*c*). For the flows investigated here, we use oceanic values of $N \approx 5.2 \times 10^{-3}\,\mathrm{s}^{-1}$, $H \approx 2000\,\mathrm{m}$ and $U_o \approx 0.1\,\mathrm{m\,s}^{-1}$ for a very large $NH/U_o \approx 100$. The response of a stratified flow varies with the height of the obstacle h_m, as governed by the topographic Froude number Nh_m/U_o. For a very small obstacle, $Nh_m/U_o \ll 1$, linear dynamics predicts that stationary lee waves over the obstacle will have the horizontal wavenumber k_x set by the dominant topographic wavenumber. The vertical wavenumber is set by the requirement that the waves be arrested, so that the magnitude of the horizontal phase speed is equal to the flow velocity: $U_o = c_{px} = N/(k_x^2 + k_z^2)^{1/2}$. If the waves are hydrostatic this simplifies to $k_z = N/U_o$.

H (m)	h_m (m)	W (km)	N (10^{-3}s^{-1})	U_o (cm s^{-1})	NH/U_o	Nh_m/U_m
2000	1000	10	5.2	1, 1.5, 2, 2.5, 3, 4, ..., 16, 17, 20, 25	1040–42	260–10.4
2000	1000	10	2.6	1, 2, 4, 8, 12, 16, 20	520–26	130–7
1300	300	10	5.2	0.8, 1.6, 2.6, 6.1, 12.3, 18.5, 24.6, 30.8	845–22	150–4
1650	650	10	5.2	4.9, 9.7, 14.6, 19.4	175–44	41–11
2000	500	10	5.2	4, 8, 12, 16, 20	260–52	49–10
2000	1500	10	5.2	2, 4, 8, 12, 16, 20	520–260	98–49

H (m)	h_m (m)	W (km)	N (10^{-3}s^{-1})	U_o (cm s^{-1})	NH/U_o	Nh_m/U_m
2000	1000	5, 7, 10, 20, 40	5.2	4	260	65
2000	1000	5, 10, 20, 40	5.2	6	173	43
2000	1000	5, 10, 20, 40	5.2	8	130	33
2000	1000	5, 10, 20, 40	5.2	10	104	26
2000	1000	5, 7, 10, 20, 40	5.2	12	87	22
2000	1000	5, 10, 20, 40	5.2	14	74	19
2000	1000	5, 7, 10, 20, 40	5.2	16	65	16

TABLE 1. Summary of external dimensional parameters for model runs discussed. The runs in the first set test the dependence on the stratification (N), obstacle height (h_m), water depth (H) and initial upstream velocity (U_o). The second set test the dependence on obstacle width (W) at a variety of flow speeds.

For finite-height obstacles with $Nh_m/U_o < 1$, nonlinear effects become important, but the flow over the obstacle is still calculable from the initial upstream conditions (Long 1955). As $Nh_m/U_o \gtrsim 1$ two effects become important. First, not all the water upstream of the obstacle can surmount the crest. This creates a convergence of dense water upstream that propagates arbitrarily far upstream as a 'columnar disturbance', changing the stratification and velocity profile relevant for predicting the downstream flow (Pierrehumbert & Wyman 1985; Baines 1988). For $Nh_m/U_o \gtrsim 3$ 'partial blocking' is observed (Farmer & Denton 1985), and some of the water upstream does not ever make it over the obstacle. This blocked water creates a stagnant layer on both the up- and downstream sides of the obstacle, with compensating accelerated flow above. For moderate Nh_m/U_o, the steady-state flow is not analytically predictable; Baines (1988) resorts to an iterative procedure, and recent work has simulated the Navier–Stokes equations numerically.

The second effect that occurs with increased nonlinearity is that streamlines downstream of the obstacle become statically unstable in a stratified hydraulic jump (Peltier & Clark 1979; Durran 1990; Afanasyev & Peltier 2001). The flow can also develop local shear instabilities where $Ri^{-1} = (\partial u/\partial z)^2/N^2 > 4$ (Peltier & Scinocca 1990; Farmer & Armi 1999). Both the turbulence mechanisms dissipate energy and cause mixing (Klymak & Gregg 2004; Inall *et al.* 2005), further invalidating Long's solution.

For the flows considered here the topographic Froude number is in the range $8 < Nh_m/U_o < 320$ (figure 1*b* and table 1), much beyond the regimes we have seen previously reported. Our study therefore extends the understanding of stratified flows over topography into a previously unexplored regime. Blocking alters the response to such an extent that we argue the relevant velocity scale to use for characterizing the local response is no longer the free-stream velocity U_0, but the mean velocity of the layer at the top of the obstacle $U_m = U_o(H/H - h_m)$. For large Nh_m/U_o, the upstream velocity in the non-blocked layers is well approximated by this velocity.

For the oceanic problems that motivate this study the mean flow oscillates with the tide (Legg & Klymak 2008). Therefore the issue of how long it takes for the flow to become 'quasi-steady' is important. For short, narrow obstacles ($Nh_m/U_o \ll 1$, $U_o/\omega_o W \gtrsim 1$, where W is the width scale of the obstacle, and ω_o the forcing frequency) the flow can be considered quasi-steady if the forcing frequency satisfies $\omega_o/N \ll 1$ (Bell 1975). This is not the case for large obstacles ($Nh_m/U_o \gtrsim 1$ or $U_o/\omega_o W \ll 1$) where blocking and upstream effects become important and the establishment time of the lee wave can become a significant multiple of $1/\omega_o$ (Pierrehumbert & Wyman 1985; Klymak & Gregg 2003). Below it is demonstrated that the establishment time can be predicted by the implied vertical group velocity, which is in turn governed by the aspect ratio of the topography.

2. Numerical model

The model used here is the MITgcm (Marshall *et al.* 1997; Legg & Klymak 2008). We use a two-dimensional topography, with a stretched horizontal coordinate system. For most of the runs here $H = 2000$ m (table 1), and vertical resolution was 200 points with $\Delta z_m = 10$ m; a few runs were made with $H = 1300$ and 1650 m. The horizontal domain was 174 km over 240 grid cells. The inner 80 grid cells were spaced 100 m apart, and then the grid was telescoped linearly so that for the outer cells $\Delta x = 2$ km. The obstacle in all cases is a Gaussian shape, with height from the seafloor given by $h = h_m \exp(-x^2/W^2)$. The width W introduces an aspect ratio to the problem $\alpha_o = h_m/W$.

The model was run in hydrostatic mode for numerical efficiency. Experiments with non-hydrostatic code did not reveal substantial differences in the features of interest here, given that our topographic aspect ratios are typically $\alpha_o = 0.1$. The boundaries were forced with a constant inflow/outflow condition of U_o. The linear stratification of $N_o = 5.2 \times 10^{-3}\,\mathrm{s}^{-1}$ was achieved by using temperature in a linear equation of state ($N_o/2$ was used for a few runs). The open boundaries allowed waves to radiate out of the domain (Orlanski 1976), and linear nudging was used in the outer 10 boundary points to suppress boundary instabilities. Flow instabilities are smoothed out by a Richardson-number turbulence scheme (Mellor & Yamada 1982) which increases diffusivities and viscosities above the background values. The background values of vertical diffusivity and viscosity are $K_v = \nu_v = 10^{-5}\,\mathrm{m}^2\,\mathrm{s}^{-1}$, while the background values of horizontal diffusivity and viscosity are $K_h = \nu_h = 10^{-3}\,\mathrm{m}^2\,\mathrm{s}^{-1}$. Convective instabilities are smoothed away with a very strong diffusivity. The Mellor & Yamada (1982) mixing dominated in the lee of the obstacle, primarily due to convective overturning. A number of experiments with different advection schemes and mixing parameterizations indicate that the large- and medium-scale features of the flow, which are the focus of our study, do not change for reasonable choices. An examination of the mixing induced by these flows is beyond the scope of this paper. Runs were made for 60 h of simulation time, or 180 buoyancy periods.

The model does not resolve the bottom boundary layer so we run with a free-slip bottom boundary condition. This rules out bottom boundary layer separation, which has been implicated in affecting the development of lee wave flows in fjords (Farmer & Armi 1999; Lamb 2004). However, laboratory flows only exhibit steady-state boundary layer separation for low Nh_m/U_o flow over steep obstacles (Baines 1995), whereas for the runs explored here Nh_m/U_o is large, and the aspect ratios relatively gentle, implying that the flow is separating because it encounters dense

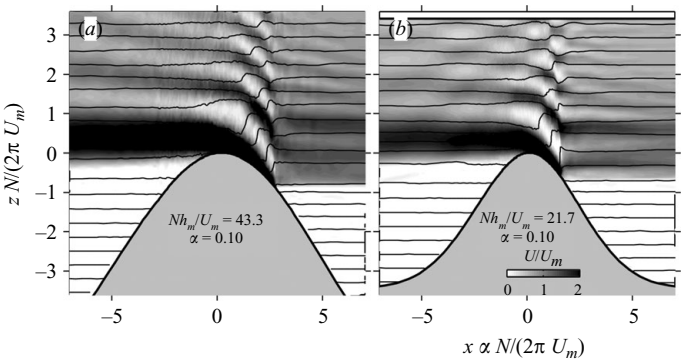

FIGURE 2. Two example steady-state flows, the flow in (*a*) is half the speed of (*b*). The vertical axis is scaled by the expected vertical wavelength and the horizontal by the expected horizontal wavelength. Thus the vertical wavelength of the flow in physical space in (*a*) is half that in (*b*). Contours are of density, evenly spaced in the upstream profile. Both obstacles have the same shape in physical space, which when non-dimensionalized means the view is only of the top of the obstacle in (*a*). Note the channel surface is plotted at the top of (*b*).

water downstream not because of torque and flow reversal in the bottom boundary layer (Klymak & Gregg 2003; Lamb 2004).

3. Results

3.1. *Example and scaling*

Two examples serve to motivate the remainder of the paper and the appropriate scaling for the flow near the obstacle crest (figure 2). Both the simulations are run for the same topography and stratification ($H = 2000$ m, $h_m = 1000$ m, $\alpha_o = h_m/W = 0.1$, $N = 5.2 \times 10^{-3}$ s^{-1}). The first (figure 2*a*) has an upstream velocity $U_0 = 0.06$ m s^{-1}, the second has double that $U_0 = 0.12$ m s^{-1}.

The steady-states in both simulations show that the water upstream of the obstacle has been arrested below the crest. The boundary conditions are such that the barotropic flow remains (approximately) constant everywhere in the domain, so the transport in the layer above the crest has the same transport as the initial condition, implying that a reasonable scaling for the velocity is

$$U_m = \frac{U_o H}{H - h_m} = \frac{U_o H}{D_m}, \tag{3.1}$$

where we have defined the depth of the water at the obstacle crest as $D_m = H - h_m$. We expect solutions in the lee of the sill that are stationary with respect to the oncoming flow. Although we do not expect our waves to be linear, we scale by the linear vertical wavelength $k_z = N/U$ for hydrostatic waves, except now $U = U_m$, instead of U_o, so that $\hat{z} = zN/2\pi U$. The utility of this scaling can be seen by inspection in figure 2 where the alternating bands of fast- and slow-moving water in the lee of the obstacle have approximately the correct wavelength. As demonstrated below, for most of the flow features we are interested in, a useful scaling for the flow is $N D_m/U_m$, form drag being the notable exception. Thus the height of the topography, h_m only matters in setting the modified upstream velocity U_m. Once it has been established, the depth of the stagnant pool does not play a dynamic role.

The horizontal scaling is given by the same vertical scale, modified by the aspect ratio $\alpha = h_m/W$ of the topography. Below we will show that the 'effective height'

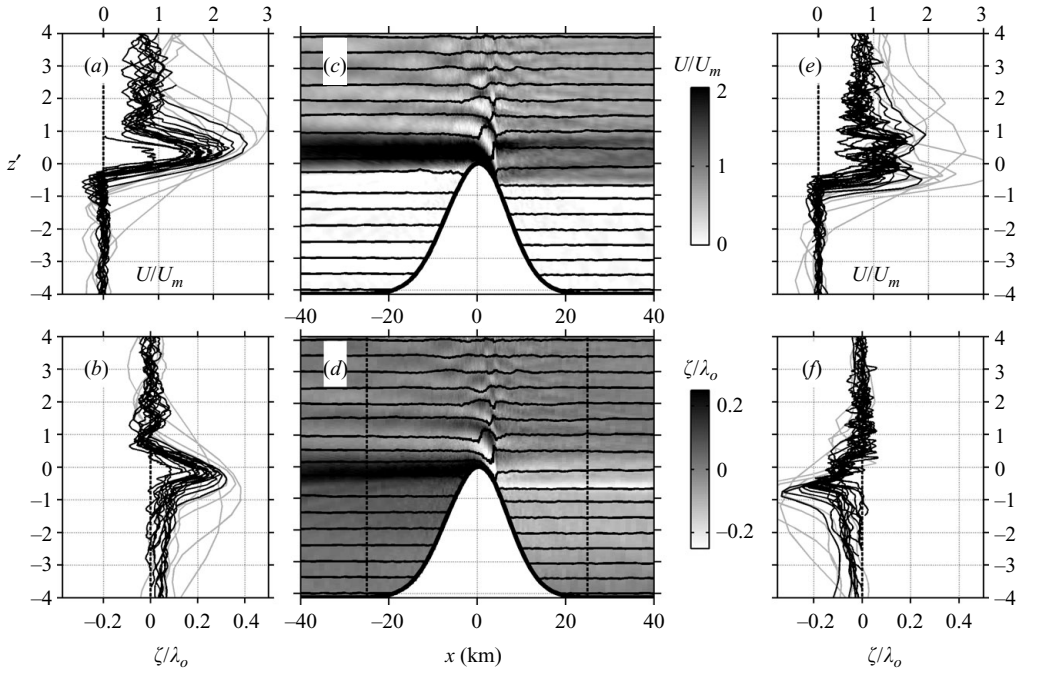

FIGURE 3. Up- and downstream profiles 25 km from the obstacle crest for all the runs in the first set of table 1, shown 180 buoyancy periods after the beginning of the calculation. The vertical is scaled as $z' = zN/(2\pi U_m)$, as discussed in the text. (*a*) Upstream velocity scaled by U_m, (*b*) upstream vertical displacement scaled by $\lambda_o = 2\pi U_m/N$. (*c*) Example velocity field, and (*d*) displacement field from a run with $Nh_m/U_m = 52$, $\alpha_o = 0.1$ both with isopycnal contours from an equispaced upstream profile. (*e*) Downstream velocity and (*f*) displacement. In (*a*), (*b*), (*e*) and (*f*) the grey profiles are for runs where high-mode waves were not expected to have propagated 25 km upstream by 180 buoyancy periods.

of the topography scales close to $\lambda_z = U/N$, so the effective width will be given by $\lambda_x = \lambda_z/\alpha$, and therefore $k_z/k_x = \alpha$.

Finally, in figure 2 and the plots that follow, U is scaled by U_m, and the temperature by $U_m N/\beta g$ where β is the thermal expansion co-efficient, and g the gravitational constant.

3.2. *Upstream and downstream response*

The response far from the obstacle is the result of columnar disturbances that propagate up and downstream after the flow is started from rest. For the high NH/U flows considered here the upstream response is relatively uniform over a broad range of ND_m/U_m when scaled by $\lambda_o = 2\pi U_m/N$ (figure 3*a*,*b*). The velocity response consists of a blocked flow deeper than the obstacle crest. At the obstacle crest there is a strong acceleration, between $1.5U_m$ and $2U_m$, this accelerated region extending approximately one wavelength above the obstacle. Above that the flow is slightly oscillatory, with the oscillations becoming more pronounced the longer the flow is allowed to develop. However, in general, the mean of this flow is centred between $0.75U_m$ and $1U_m$.

We can empirically parameterize the variations of these velocities as they change with the forcing, ND_m/U_m (figure 4). For the mean velocity (u_a) above the first vertical

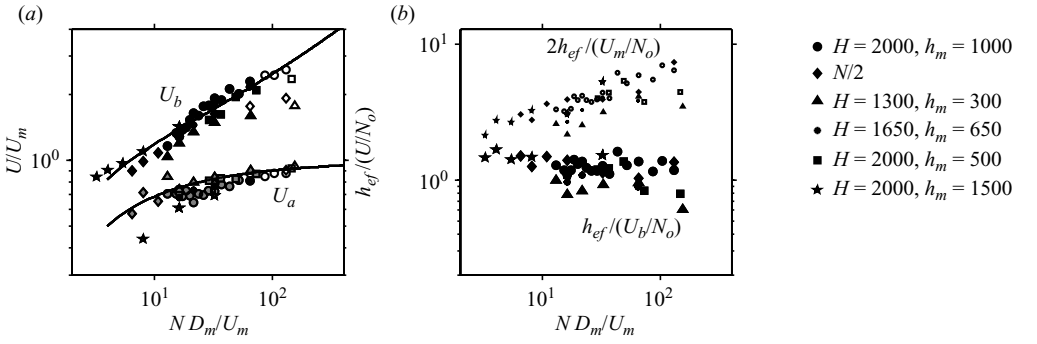

FIGURE 4. (*a*) Scaling of the upstream velocity. Black dots are the mean of the velocity in the first vertical wavelength above the obstacle crest (u_b) and grey dots are the mean velocity of the water column above (u_a). See the text for the fits. (*b*) Depth below the crest that water is withdrawn from the upstream reservoir (h_e) scaled by U_m/N_o (small symbols) and u_b/N_o (large symbols).

wavelength ($z - D_m > \lambda_o$) a simple fit:

$$\frac{u_a}{U_m} = 1 - \left(\frac{N D_m}{U_m}\right)^{-1/2} \tag{3.2}$$

is chosen to asymptote to $u_a = U_m$ for large $N D_m/U_m$ where the vertical wavelength becomes very small, though we did not test this limit thoroughly as we do not expect it to be important in realizable flows. The mean of the velocity in the first wavelength u_b follows from this as

$$u_b \lambda_o + u_a(D_m - \lambda_o) = U_m D_m, \tag{3.3}$$

which gives

$$\frac{u_b}{U_m} = \frac{N D_m}{U_m}\frac{1}{2\pi}\left(1 - \frac{u_a}{U_m}\right) + \frac{u_a}{U_m}, \tag{3.4}$$

parameterizing the upstream response in the first vertical wavelength (figure 4).

The changes in the upstream velocity are mediated by changes in the upstream density field, and thus internal pressures. These are concentrated within two wavelengths of the obstacle crest (figure 3*b*,*d*), and quantified using the vertical displacement of isopycnals from their initial depth $z_o(T)$:

$$\zeta(z) = z - z_o(T(z)). \tag{3.5}$$

The largest upward displacements occur just below the obstacle crest and have a value near $0.25\lambda_o$. The highest this disturbance reaches above the crest is approximately λ_o. Above this height there are vertical displacements, but they are small. Downstream, there is a region almost $-\lambda_o$ below the obstacle crest where the water has been drawn down as much as $0.25\lambda_o$, but again there are only small displacements above λ_o.

The depth from which water is withdrawn from the upstream reservoir can be thought of as an effective height of the topography h_{ef}. This scales with the upstream velocity and stratification $h_{ef} = U/N$ (Stommel & Farmer 1953). If we use U_m as the velocity scale, h_{ef} is under predicted (figure 4*b*, small symbols, though note these are offset by a factor of 2 for ease of display). A second-order correction using the flow speed near the obstacle crest u_b gives a better scaling (figure 4*b*, large symbols).

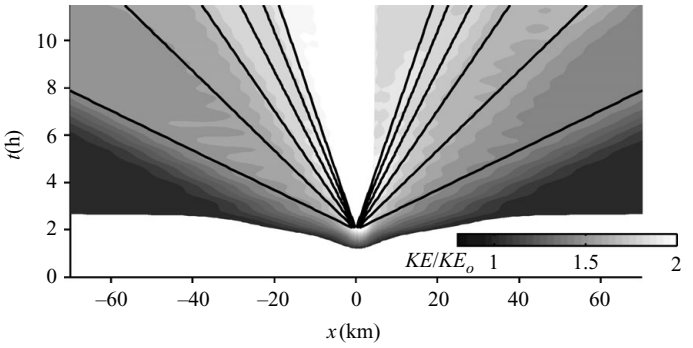

FIGURE 5. Propagation of up- and downstream signals from the obstacle crest ($Nh_m/U_m = 52$) quantified by the depth-integrated kinetic energy divided by the initial kinetic energy $HU_o^2/2$. Lines at angles indicate the path that signals with the deep-water mode 1–6 linear wave speeds (c_n) in a quiescent fluid ($c_n \gg U$) would take if they started at $t = 2$ h, the end of the spin-up period.

Hydraulic control of a flow means that the energy up- and downstream is permanently changed by introduction of the obstacle, usually because the initial flow configuration does not have enough kinetic energy to surmount the obstacle. Simple flows have readily calculable critical conditions (i.e. Henderson 1966; Armi 1986), and usually involve an arrested wave speed. Here, the flow is more complex, and a stratified critical criterion is not as readily identified. Nonetheless we can observe the irreversible change of the upstream energy. For simplicity, we just consider the kinetic energy here, $Ke = \int_0^H 1/2\ u^2\,\mathrm{d}z$ compared to the undisturbed kinetic energy $Ke_o = 1/2\ U^2 H$ (figure 5). The response is somewhat smeared because of the 2 h spin-up of the simulations, but the earliest response follows the mode 1 wave speed and subsequent increases in the response follow the lower mode speeds. These changes are 'columnar' in that they do not oscillate in time (though the astute reader will note some oscillations, primarily due to undamped barotropic waves), a signature of a hydraulic response.

3.3. *Form drag*

The up- and downstream responses are characterized by a lift of the isopycnals upstream and a drop downstream, leading to a pressure drop across the obstacle. This pressure drop is the manifestation of a form drag F_d on the mean flow:

$$F_d = \int_{-\infty}^{+\infty} P_h \frac{\mathrm{d}h}{\mathrm{d}x}\,\mathrm{d}x, \tag{3.6}$$

where P_h is the pressure at the seafloor. The displacements are consistent enough across the runs that we can derive a simple scaling for the form drag using a two and a half-layer model that has the vertical displacements noted above. We assume that at some height above the topography h_u the water is undisturbed (see sketch, figure 6*c*), and that an interface initially at $-\Delta h/2$ has been raised $\Delta h/2$ upstream to the obstacle crest and dropped $-\Delta h/2$ downstream. For constant stratification there is a density difference in the two layers of $\Delta\rho = \rho N^2(h_m + h_u)/2g$ and the predicted

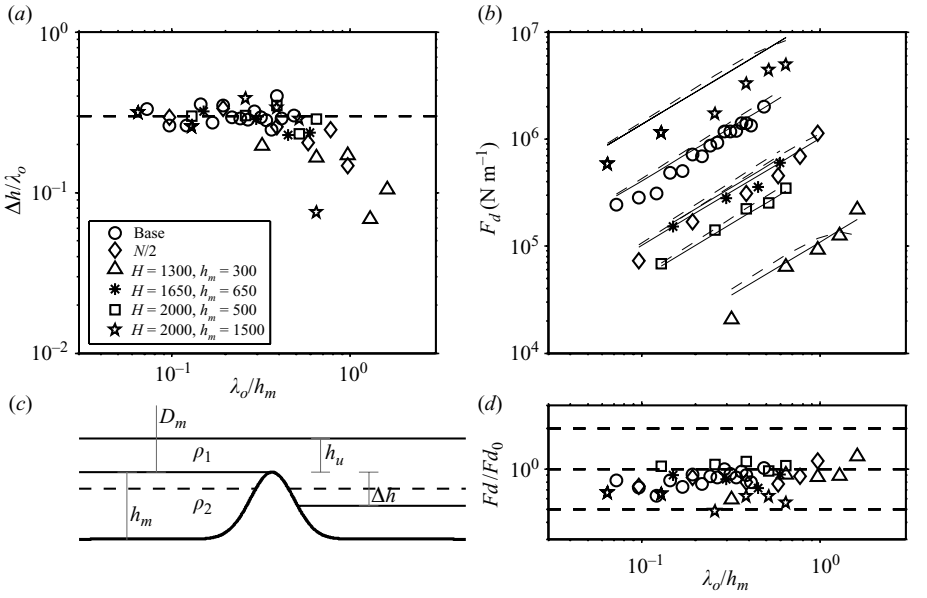

FIGURE 6. (*a*) Downstream drop of the isopycnal at the obstacle crest as a function of $\lambda_o/h_m = 2\pi U_m/Nh_m$. (*b*) Dimensional form drag F_d of flows for a variety of flow states (units are N m^{-1}). Solid lines are the simple theory discussed in the text, dashed has higher order terms. (*c*) Definition sketch for form drag calculation. (*d*) Ratio between predicted form drag F_{d_0} and actual form drag F_d.

form-drag F_{d_0} is

$$F_{d_O} = \int_{-h_m}^{-\Delta h} g\,\Delta\rho\,\Delta h\,\mathrm{d}h + \int_{-\Delta h}^{0} g\,\Delta\rho\,h\,\mathrm{d}h, \tag{3.7}$$

$$= g\,\Delta\rho\,\Delta h\,\left(h_m - \frac{3}{2}\Delta h\right), \tag{3.8}$$

$$= \frac{\rho N^2}{2}\Delta h\,h_m^2\left(1 + \frac{h_u}{h_m} - \frac{3}{2}\frac{\Delta h}{h_m} - \frac{3}{2}\frac{h_u}{h_m}\frac{\Delta h}{h_m}\right). \tag{3.9}$$

To leading order the form drag depends on the stratification, obstacle height and the up- and downstream displacement $\Delta h \approx \lambda_o/3$ (figure 6*a*). There is a first-order correction due to $\Delta h/h_m$ and h_u/h_m. For simplicity, we assume that $h_u \approx \lambda_o = 2\pi U_m/N$ to get

$$F_{d_O} = \rho N U_m h_m^2 \frac{\pi}{2}\left(1 + \pi\frac{U_m}{Nh_m} - 2\pi^2\left(\frac{U_m}{Nh_m}\right)^2\right), \tag{3.10}$$

where the last two terms can be ignored for $Nh_m/U_m \gg \pi/2$, or $\lambda_o/h_m \ll 4$ which is true for most of the runs studied here.

This scaling works well for predicting the form drag on the obstacle (figure 6*b*, calculable precisely from the model output), though it overpredicts the drag by 20 % or so for most obstacles (figure 6*d*). The largest overprediction is for the ridges with $h_m/H = 0.75$ (stars), and thus the ridges for which the upstream response was most influenced by the presence of the upper boundary. This is to be expected since our scaling did not account for the effect of the upper boundary. A similar scaling does

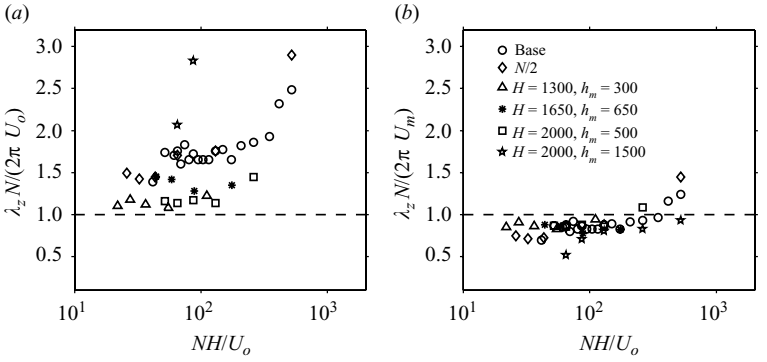

FIGURE 7. Vertical wavenumber of lee waves at $tN = 180$ and $x/W = 0.16$ compared to (a) the initial velocity and (b) the predicted upper layer velocity U_m. Note for the abscissa we have used the initial NH/U_o in both cases. Low-speed runs with short wavelengths $\lambda_z < 3\Delta z$ are not shown, where Δz is the model resolution.

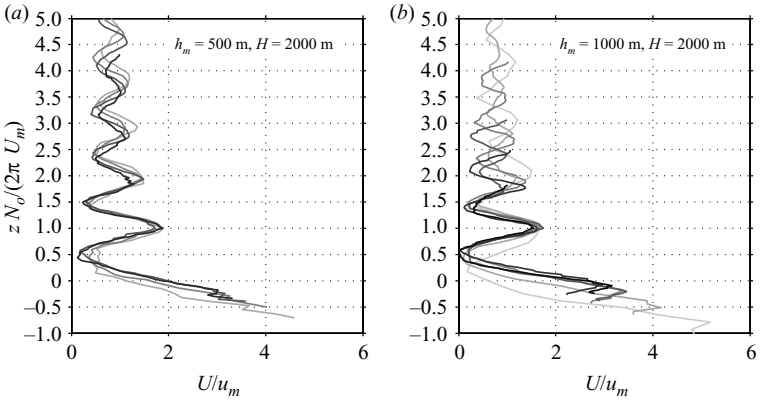

FIGURE 8. Velocity profiles for a number of runs at position $x/W = 0.16$ downstream of the obstacle crest, aligned so the second maxima are at the same depth in non-dimensionalized space. Profiles are shown for (a) $h_m/H = 1/4$ (all the runs in table 1, row 5) and (b) $h_m/H = 1/2$ (table 1, row 1). Darker curves are for faster flows (smaller Nh_m/U_m).

not exist for low-NH/U flows because the up- and downstream responses are not as predictable.

3.4. *Steady lee response*

The lee response is dominated by an arrested wave. The vertical wavelength λ_z is determined from the velocity signal in the lee of the obstacle at a dimensionless distance $x/W = 0.16$ from the crest by finding the second peak of the lag autocorrelation and then compared to $2\pi U/N$. The wavelength of the lee-wave disturbance scales with the upstream velocity, $U = U_m$, much better than with the original velocity (figure 7).

These lee 'waves' are very nonlinear, so this scaling only holds in a rough sense, however, it does a relatively good job of collapsing the response as observed in velocity profiles slightly downstream of the crest (figure 8). The first half-wavelength tends to be larger than the ones further aloft, with the first velocity maximum near

1.5-λ_o. This is the most nonlinear part of the lee response, and has the strongest velocities.

The presence of the free surface also affects the lee response at higher order. For a short obstacle, where the free surface is far from the obstacle crest, the scaling holds up the best (figure 8*a*). The wavelengths further aloft, i.e. greater than $3\lambda_o$, are somewhat shorter than the scaling predicts. When the obstacle is half the water depth (figure 8*b*) the universality of the velocity profiles is not as robust. The faster flows (darker curves) have fewer wavelengths that fit in the water depth, and the influence of the surface changes the regularity of the response. This implies that the scalings here work best when at least one vertical wavelength fits in the gap, $ND_m/U_m > 2\pi$.

3.5. *Establishment time*

Geophysical lee waves are not always formed under steady forcing, therefore the time it takes for the lee wave to become established is important to determining if it will be seen in natural flows. We scale the growth of the lee response by considering the vertical propagation speed of the waves. The vertical group speed of a linear wave is given by $c_{gz} = \partial\omega_i/\partial k_z$, where $\omega_i = Nk_x/k_z$ is the intrinsic frequency of the hydrostatic wave. This gives $c_{gz} = -Nk_x/k_z^2$. For linear waves, as noted above, k_x and k_z are independent, and set by the width of the obstacle and the N/U respectively. This gives $c_{gz} = 2\pi(U^2/WN)$, and if we define a time scale to create a lee wave as the time it takes for a signal to propagate one vertical wavelength, we get $\hat{t} = (U/W)t$.

This linear scaling, however, does not apply to the growth of the lee waves in the highly blocked case discussed here. A few examples demonstrate the scaling problem (figure 9). Figures 9(*a*) and 9(*g*) are taken at the same time in the simulations, with the width W held constant, but U_m is greater in figure 9(*a*) than in figure 9(*g*). These two simulations appear almost identical despite the linear scaling predicting that the faster flow should have evolved more.

The reason why the linear scaling fails is because for the strongly blocked case, the 'effective width' of the topography is set by the 'effective height' h_e, and therefore k_x depends on k_z. As shown above, $h_{ef} \approx 4U_m/N$, so if the aspect ratio near the crest is α_{ef}, $k_x \approx (\alpha_{ef}N)/U_m$ and $c_{gz} \approx U_m\alpha_{ef}$. This leads to a non-dimensionalization for these flows of

$$\hat{t} = \frac{N\alpha_{ef}}{2\pi}t. \tag{3.11}$$

The aspect ratio near the crest depends on the shape of the obstacle. For Gaussian topography,

$$\alpha_{ef} = \frac{h_{ef}}{x(h_m - h_{ef}) - x(h_m)}, \tag{3.12}$$

$$= \frac{h_{ef}}{W}\left(-\ln\left(1 - \frac{h_{ef}}{h_m}\right)\right)^{-1/2}. \tag{3.13}$$

Note that for a Gaussian, or any convex obstacle, $\alpha_{ef} < h_m/W$.

A few examples demonstrate this scaling (figure 9). A wide ridge takes longer in non-dimensionalized time to become established than a narrow ridge (figure 9*a–c* compared to figure 9*d–f*). Conversely a slower flow (figure 9*g–i*) sets up almost as quickly as the fast one (figure 9*a–c*). It is a little slower because α_{ef} is smaller in the slow flow case. Finally, a flow with $N = N_0/2$ (figure 9*j–l*) sets up more slowly than a high-stratification flow (figure 9*a–c*). However, it is not quite half as slow because the low N means h_{ef} is twice as large and therefore α_{ef} is larger for this flow.

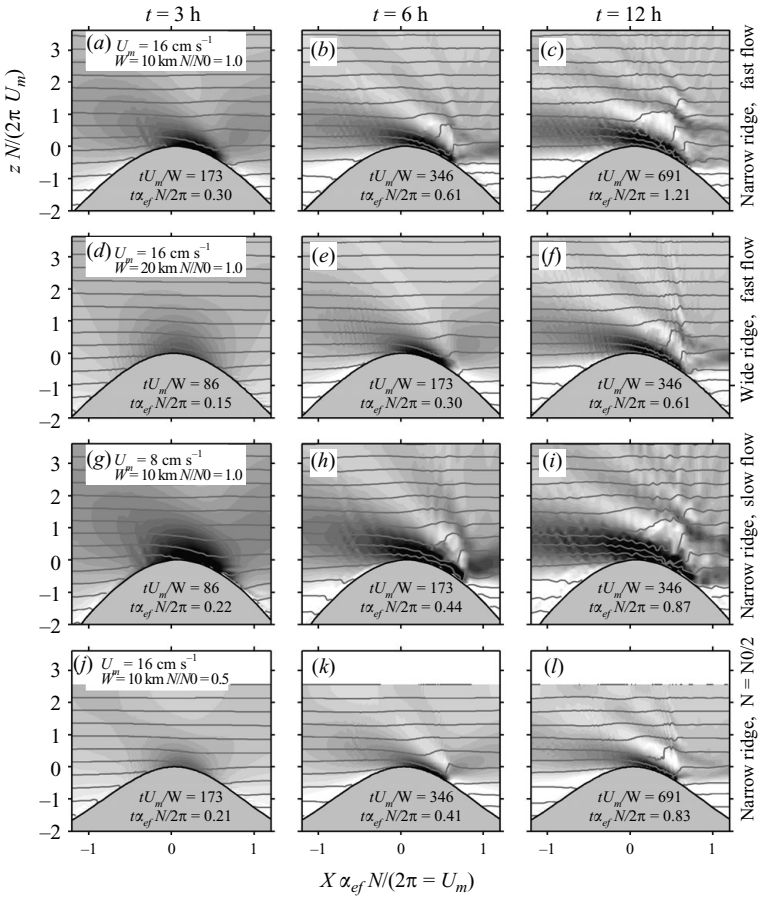

FIGURE 9. Snapshots from four runs. The first two rows are runs made with $Nh_m/U_m = 16.2$, but with a wider obstacle in the second row (*d–f*). The third row (*g–i*) is a run with the same obstacle as the first run, but with a slower flow $Nh_m/U_m = 21.7$, and the last is the same obstacle with $N = N0/2$. The run with the shallower obstacle evolves approximately half as fast as the steeper one (*d–f* compared with *a–c*). The slower flow (*g–i*) appears to evolve slightly more slowly than the faster (*a–c*), but in general they grow at the same rate. Finally the lower stratification flow (*j–l*) grows slower than higher stratification (*a–c*). See text for description of α_{ef}.

This scaling can be quantified more clearly with Hovmöller diagrams taken at $x/W = 0.2$ downstream of the obstacle crest (figure 10). For the various flows the first three local minima of velocity are traced. These propagate downwards and arrive at their resting level, in most cases by 15 h into the simulation. The speed with which this happens varies by stratification and α_{ef} (figures 10*d* and 10*i*), however, when time is scaled by $N\alpha_{ef}$ the development appears similar for all the runs (figures 10*e* and 10*j*).

Finally, we test for all the $N = N_0$ runs by checking that $c_{gz} \approx \alpha_{ef} U_m$. Energy profiles at $x/W = 0.25$ (figure 11*a*) are considered for different initial flow speeds and aspect ratios (second set of runs in table 1). There is some subjectivity to picking the upwards propagation of the lee waves; here it is tracked by the linear internal wave energy $E = (1/2)\,u'^2 + 0.5\zeta^2 N^2$ where u' is the velocity difference from the barotropic velocity and ζ is the vertical displacement. For plotting we normalize by $U_o^2/2$. The time when

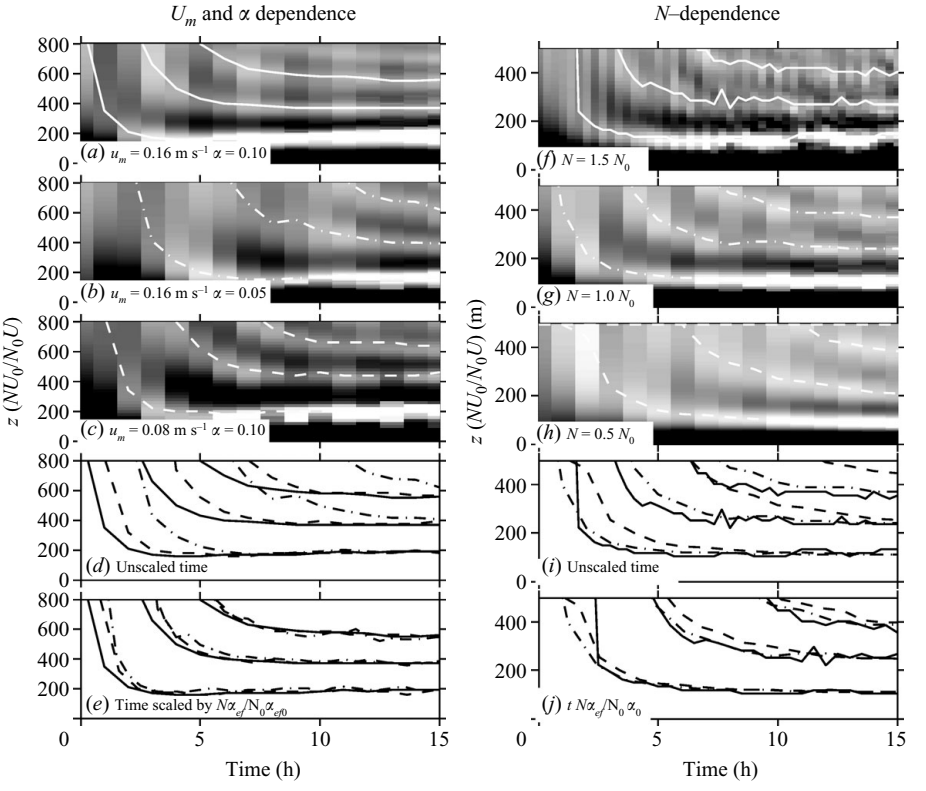

FIGURE 10. Hovmöller diagrams of u/U_m from $x/W = +0.2$ to demonstrate the rate at which the lee waves grow. In each Hovmöller diagram the first three velocity minima are traced as they propagate downwards towards the obstacle. (*a–f*) demonstrate the effect of changing α_{ef} and U_m; N is held constant. Flow over wide ridges (*b*) develops more slowly than flow over narrow (*a*). Scaling time by α_{ef} brings the time scales into agreement (*e*, solid compared to dashed-dot lines). Faster flows also develop somewhat more quickly than slower flows (*a* compared to *c*), again scaling by α_{ef} reconciles these differences (*e*). Panel (*f–j*) demonstrates that there is a stratification dependence to the development of the flow that scales linearly with $N\alpha_{ef}$ (*j*).

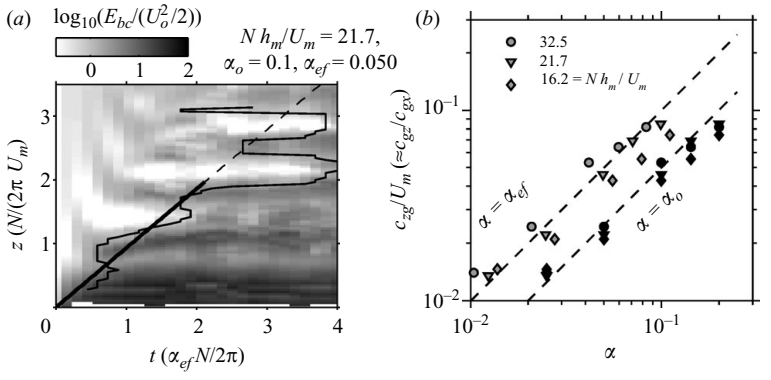

FIGURE 11. (*a*) Example of determining vertical wave speed from energy at $x/W = 0.25$. Time is scaled by the effective aspect ratio and the vertical axis by the vertical wavelength scale. (*b*) Comparison of vertical wave speed scaled by the velocity scale U_m for runs with different obstacle widths (α_o) and the same wave speeds compared to the effective aspect ratio (α_{ef}).

the energy exceeds half of its eventual maximum is chosen to represent when upward propagating energy first passes a depth (thin line in figure 11*a*). This measure of the location of the energy front was then fit over the first two wavelengths ($z/\lambda_o < 2$) to arrive at a measure of c_{gz}. Above the first two wavelengths it was difficult to fit the propagation because nulls in the energy were made noisy by the addition of higher mode waves as they propagated through the system. However, the non-nulls in the energy followed the fit quite well above the initial two wavelengths for most of the cases.

This procedure was applied to three different values of Nh_m/U_m and five different aspect ratios (figure 11*b* and table 1) and compared to the object aspect ratio $\alpha_o = h_m/W$ and the 'effective aspect ratio' α_{ef}. The results demonstrate good agreement with $c_{gz} = \alpha_{ef} U_m$ across this range of flows.

Note that the linear time scale is still a horizontal time scale $t_h = W_{ef}/U_m$. This is roughly the time it takes to bring dense water from the upstream side of the obstacle to the downstream side, setting the bottom boundary condition on the flow above. For the flows considered here $t_h/t_v = Nh_{ef}/2\pi U_m \approx 1/4$, so the flow translates across the effective topography in one-quarter of the time it takes for the dominant disturbance to propagate one wavelength in the vertical, and t_h therefore does not strongly affect the development of the flow. This will not necessarily be the case if the obstacle has a large plateau at the top, where the appropriate aspect ratio of the lee wave would be the slope of the sides, but the horizontal advection time scale would be set by the width of the plateau. We do not explore this regime here.

4. Conclusions and discussion

We have explored stratified flow over an obstacle for high values of NH/U_o and Nh_m/U_o, a parameter regime not previously considered. A simple scaling for the velocity is $U_m = U_o H/D_m$, and the flow is characterized by the parameter NU_m/D_m. This scaling is not possible for moderate values of Nh/U such as those considered by Baines (1988) because those flows do not have readily predictable upstream velocity scales or stratification. In the present parameter regime, the upstream stratification does not change very much, but the velocity does, with a deep stagnant layer forming on either side of the obstacle, and correspondingly faster flow above. An arrested lee wave in this increased flow has an observed wavelength close to $\lambda_o \approx 2\pi U_m/N$. The form drag on the obstacle is set by the upstream and downstream isopycnal displacements, and not by the details of the lee waves.

Establishment times are faster for steeper obstacles because the vertical group speed is proportional to αU_m, where $\alpha = h_m/W$ is the aspect ratio of the obstacle, leading to the scaling of the time as $\hat{t} = tN\alpha/2\pi$. The exact choice of α depends on how much α changes near the obstacle crest. Linear dynamics has $\hat{t} = tW/U$, so this scaling with the aspect ratio is unique to these blocked high-Nh_m/U_o flows. Clearly, there is a transition between the highly blocked time scale and the linear time scale for moderate Nh_m/U_o that we do not explore here.

It is of note that even the modified flow is still quite nonlinear. If we consider the stagnant layer upstream of the crest to be like a virtual topography, the effective obstacle height is given by the withdrawal depth, which was close to $\Delta h/2 = 0.3\pi U_m/N$ (figure 6*a*). That means that the new $Nh/U \approx 1$, and predicting the downstream flow beyond our quasi-linear scaling here is still not tractable by Long's solution.

The scaling of the lee wave growth with topographic aspect ratio is unique. The only study that we are aware of that has investigated the time dependence of a lee-wave

flow on topographic shape (Miller & Durran 1991) quantified time-dependence using the maximum flow on the topography, which is of interest to meteorologists. The time-dependence of this measure was relatively insensitive to topographic shape, and is consistent with the simulations made here (compare the maximum velocities in figures 9*a* and 9*d*). However, in the ocean we are interested in the turbulence driven by the hydraulic response, and that requires vertical propagation to become established, which we show depends on the slope.

Our results imply that it takes $\Delta t = 2\pi(\alpha_{ef} N)^{-1}$ for the first wavelength response to form. Legg & Klymak (2008) considered slopes with $\alpha_{ef} = 1/10, 1/20$ and $1/40$, and $N = 2.4 \times 10^{-3}\ \mathrm{s}^{-1}$, yielding $\Delta t = 1.9, 3.7$ and 7 h. Strong unidirectional flow in these simulations lasted half a tidal period, or 3–4 h, so according to this scaling, the steepest solution could develop a response that propagated almost two vertical wavelengths before the flow changed, similar to what was found in the simulations. The shallower slopes in the oscillating simulations did not have well-formed lee responses because the disturbance was not able to propagate high enough in the water column before the tide reverses. Of course, an oscillating tidal flow also has a history, whereby the flow set-up during one phase of the tide affects the flow later in the tide (Klymak & Gregg 2003), an effect also believed to be important in atmospheric flows (Chen, Durran & Hakim 2005).

Thanks to Chris Garrett and Eric Kunze for very helpful comments, and for the constructive criticisms of the three anonymous reviewers. This work was partially supported by the U.S. Office of Naval Research (programs N00014-08-1-1039, N00014-08-1-0376) and the Canadian NSERC Discovery Grant programme.

REFERENCES

Afanasyev, Y. D. & Peltier, W. R. 2001 On breaking internal waves over the sill in Knight Inlet. *Proc. R. Soc. Lond.* A **157** (1–27).

Armi, L. 1986 The hydraulics of two layers with different densities. *J. Fluid Mech.* **163**, 27–58.

Baines, P. G. 1988 A general method for determining upstream effects in stratified flow of finite depth over a long two-dimensional obstacle. *J. Fluid Mech.* **188**, 1–22.

Baines, P. G. 1995 *Topographic Effects in Stratified Flows*. Cambridge University Press.

Bell, T. H. 1975 Lee waves in stratified flows with simple harmonic time dependence. *J. Fluid Mech.* **67**, 705–722.

Chen, C.-C., Durran, D. R. & Hakim, G. J. 2005 Mountain-wave momentum flux in an evolving synoptic-scale flow. *J. Atmos. Sci.* **62**, 3213–3231.

Durran, D. R. 1990 Mountain waves and downslope winds. In *Atmospheric Processes Over Complex Terrain*, *Meteorological Monographs* (ed. W. Blumen), vol. 23, pp. 59–81. American Meteorological Society.

Farmer, D. M. & Armi, L. 1999 Stratified flow over topography: the role of small scale entrainment and mixing in flow establishment. *Proc. R. Soc. Lond. Ser.* A **455**, 3221–3258.

Farmer, D. M. & Denton, R. A. 1985 Hydraulic control of flow over the sill in Observatory Inlet. *J. Geophys. Res.* **90** (C5), 9051–9068.

Farmer, D. M. & Smith, J. D. 1980 Tidal interaction of stratified flow with a sill in Knight Inlet. *Deep Sea Res.* A **27**, 239–245.

Henderson, F. M. 1966 *Open Channel Hydraulics*. Macmillan.

Inall, M. E., Rippeth, T., Griffiths, C. & Wiles, P. 2005 Evolution and distribution of tke production and dissipation within stratified flow over topography. *Geophys. Res. Lett.* **32**, L08607, doi:10.1029/2004GL022289.

Klymak, J. M. & Gregg, M. C. 2003 The role of upstream waves and a downstream density-pool in the growth of lee-waves: stratified flow over the Knight Inlet sill. *J. Phys. Oceanogr.* **33** (7), 1446–1461.

Klymak, J. M. & Gregg, M. C. 2004 Tidally generated turbulence over the Knight Inlet sill. *J. Phys. Oceanogr.* **34** (5), 1135–1151.

Klymak, J. M., Pinkel, R. & Rainville, L. 2008 Direct breaking of the internal tide near topography: Kaena Ridge, Hawaii. *J. Phys. Oceanogr.* **38**, 380–399.

Lamb, K. G. 2004 On boundary layer separation and internal wave generation at the Knight Inlet sill. *Proc. R. Soc. Lond.* A **460**, 2305–2337.

Legg, S. & Klymak, J. M. 2008 Internal hydrualic jumps and overturning generated by tidal flow over a steep ridge. *J. Phys. Oceanogr.* **38**, 1949–1964.

Levine, M. D. & Boyd, T. J. 2006 Tidally-forced internal waves and overturns observed on a slope: results from the HOME survey component. *J. Phys. Oceanogr.* **36**, 1184–1201.

Lilly, D. K. 1978 A severe downslope windstorm and aircraft turbulent event induced by a mountain wave. *J. Atmos. Sci.* **35**, 59–77.

Long, R. R. 1955 Some aspects of the flow of stratified fluids. III. Continuous density gradients. *Tellus* **7**, 341–357.

Marshall, J., Adcroft, A., Hill, C., Perelman, L. & Heisey, C. 1997 A finite-volume, incompressible Navier–Stokes model for studies of the ocean on parallel computers. *J. Geophys. Res.* **102** (C3), 5753–5766.

Mellor, G. L. & Yamada, T. 1982 Development of a turbulence closure model for geophysical fluid problems. *Rev. Geophys. Space Phys.* **20**, 851–875.

Miller, P. P. & Durran, D. R. 1991 On the sensitivity of downslope windstorms to the asymmetry of the mountain profile. *J. Atmos. Sci.* **48**, 1457–1473.

Nash, J. D., Alford, M. H., Kunze, E., Martini, K. & Kelley, S. 2007 Hotspots of deep ocean mixing on the oregon continental slope. *Geophys. Res. Lett.* **34**, L01605, doi:10.1029/2006GL028170.

Orlanski, I. 1976 A simple boundary condition for unbounded hyperbolic flows. *J. Comput. Phys.* **21**, 251–269.

Peltier, W. R. & Clark, T. L. 1979 The evolution of finite-amplitude waves. Part II. Surface wave drag and severe downslope windstorms. *J. Atmos. Sci.* **36**, 1498–1529.

Peltier, W. R. & Scinocca, J. F. 1990 The origin of severe downslope windstorm pulsation. *J. Atmos. Sci.* **46**, 2885–2914.

Pierrehumbert, R. T. & Wyman, B. 1985 Upstream effects of mesoscale mountains. *J. Atmos. Sci.* **42** (10), 977–1003.

Stommel, H. & Farmer, H. G. 1953 Control of salinity in an estuary by a transition. *J. Mar. Res.* **12** (1), 13–20.